PAPER

Cu₂O nanoparticles anchored on carbon for the efficient removal of propofol from operating room wastewater *via* peroxymonosulfate activation: efficiency, mechanism, and pathway†

Yujie Tang, [iD] *[a] Shiyin Zhao,[b] Zemin Peng,[a] Zhen Li,[a] Liang Chen[a] and Pei Gan*[a]

Anesthetic drug wastage has increasingly become the main resource of operating room sewage, which poses a great risk to the safety of humans and other organisms. Propofol is the most widely used anesthetic drug in the world, and also occupies the largest proportion of the total anesthetic wastage in the operating room. In this work, a 2D Cu₂O anchored carbon catalyst (Cu₂O@NC) was prepared by the assembly-pyrolysis process and successfully applied to peroxymonosulfate (PMS) activation. We took propofol as a typical example and investigated the removal activity through heterostructure-enhanced advanced oxidation processes (AOPs). Through the degradation process, propofol can be removed from 20 ppm to ultralow levels within 5 min using the PMS/Cu₂O@NC system. The degradation pathway of propofol was deduced through quantum chemical calculation and LC/GC-MS results. The final products were verified as CO_2 and H_2O. Moreover, sulfate radicals ($SO_4^{•-}$) proved to be the dominant reactive oxidation species by radical scavenger experiments and ESR results. In addition, it has great universality for various pharmaceuticals such as tetracycline (TC), amoxicillin (AMX), cephalexin (CPX), and norfloxacin (NFX). Our work provided the possibility to treat operation room sewage in a rapid, high-efficiency, and feasible way.

Introduction

Anesthetics have increasingly become one of the most common pharmaceutical pollutants in operating room sewage due to their wide use in clinical practice.[1–3] Propofol is the world's most widely used intravenous general anesthetic.[4–6] However, a large amount of discarded and excreted propofol directly enters the aquatic environment without efficient treatment.[7] According to reports, wasted propofol accounts for 45% of the total waste of pharmaceuticals in the operating room.[8–10] Propofol could hardly be massively photolyzed or biodegraded under ambient conditions,[8,11,12] but may directly lead to the death of algae, small crustaceans, and freshwater fish.[13,14] Simultaneously, propofol presents bioaccumulating properties in highly tolerant organisms due to its fat solubility and then reach the species at the top of food chain step by step.[15,16] Moreover, propofol also exhibits outstanding thermal stability. Only when the ambient temperature is higher than 1000 °C for 2 seconds, the drug can be incinerated.[14] Hence, the continued release of propofol has great potential to become a persistent organic pollutant in the

ecosystem. However, studies on the removal of propofol, degradation mechanism and pathway are sparse. Hence, efficient strategies for the treatment of propofol wastage are urgently needed.

The techniques for removing pharmaceutical pollutants from water bodies can be summarized into four types: membrane separation,[17,18] chemical decomposition,[19,20] adsorption,[21,22] and photocatalysis.[23,24] However, these techniques always have shortcomings such as low efficiency, environmental unfriendliness and high cost in practical operation.[12,25] Among all techniques, the advanced oxidation process (AOP) has received considerable attention for its highly efficient, low-cost, and environmentally friendly characteristics.[26–28] Conventional catalysts for the oxidants are transition metal oxides, however, they also show a small specific surface area, poor porosity, and low-efficiency active sites. MOFs and their derivatives have received extensive attention from researchers for their outstanding performance in various applications, such as sensing adsorption, photocatalysis, drug delivery and energy storage.[21,29–31] Meanwhile, due to the changeable chemical composition, large specific surface area, and controllable pore size, the MOFs derived heterostructure is an ideal activator for PMS.[32–35]

Herein, a reported Cu–TCPP nanosheet was subjected to produce a heterostructure catalyst that could efficiently activate PMS in the degradation of propofol.[21] After assembly for 24 h

[a]Hunan Provincial Maternal and Child Health Care Hospital, Changsha 410008, P. R. China. E-mail: tangyujie0202@163.com; hnsfybjymz@yahoo.com

[b]Faculty of Health Sciences, University of Macau, Macau SAR 999078, P. R. China
† Electronic supplementary information (ESI) available. See DOI: 10.1039/d1ra03049c

and then pyrolyzing at 450 °C for 2 h under N_2 atmosphere, the 2D catalyst was successfully prepared. The XRD pattern and the TEM image showed that the catalyst was composed of Cu_2O loaded on 2D N-doped carbon. Significantly, under optimized conditions, $PMS/Cu_2O@NC$ could remove propofol from 20 mg L^{-1} concentration to an ultra-low level. The main byproduct was proved to be cyclohexanone according to LC/GC-MS, and the final degradation products were CO_2 and water according to TOC results. The sulfate radical ($SO_4^{\cdot-}$) played a dominant role during the degradation process. The quantum chemistry calculation was also employed to verify the degradation path and degradation possibility of propofol. Simultaneously, $PMS/Cu_2O@NC$ presented universality for other pharmaceutical contaminants such as tetracycline (TC), amoxicillin (AMX), cephalexin (CPX), and norfloxacin (NFX). This work provides great potential for AOPs to be widely used for sewage treatment coming from operating rooms.

Experimental

Materials

Meso-tetra(4-carboxyphenyl)porphine (TCPP, Fig. S1†) was bought from Yanshen Technology (Jilin, China). PMS, propofol, TC, AMX, CPX, NFX, copper nitrate trihydrate [$Cu(NO_3)_2 \cdot 3H_2O$], N,N-dimethylformamide (DMF), ethanol and *tert*-butanol were purchased from Aladdin Chemical (Shanghai, China). All reagents and solvents were used as received without any purification.

Characterizations

Powder X-ray diffraction (XRD) patterns were recorded using a polycrystalline diffractometer (Rigaku D/max-2550 VB) with Cu Kα ($\lambda = 0.154$ nm). The Fourier transform infrared spectrometer (FTIR) (Nicolet 1S 50) with KBr pellets was used for analysis. The morphology was recorded using field emission scanning electron microscopy (SEM, Zeiss Merlin) with a working voltage of 10 kV and transmission electron microscopy (TEM, Tecnai F30) with an acceleration voltage of 300 kV. The thermogravimetric analysis and differential scanning calorimetry (TG-DSC) were performed on a Setsys EVO Easy 1750 (SETARAM). X-ray photoelectron spectroscopy (XPS) was measured using a Thermo ESCALAB 250XI instrument equipped with Al Kα radiation. The surface area and porosity were analyzed by Micromeritics ASAP2046. The electron spin-resonance (ESR) spectra were recorded by a JES FA200 spectroscopy.

Preparation of $Cu_2O@NC$

The Cu–TCPP nanosheet was synthesized by a reported method.[21] Typically, 93.7 mg $Cu(NO_3)_2 \cdot 3H_2O$ and 98.5 mg TCPP were dissolved in 50 mL DMF in a reactor. After ultrasonication for 10 minutes, the reactor was transferred to an oven with a working temperature of 100 °C for 24 h. The resulting dark red precipitate was washed several times with DMF and ethanol and then dried in an oven at 60 °C for 8 h. The resulting Cu–TCPP samples were stored for further use.

The as-prepared Cu–TCPP nanosheets were subjected to prepare metal-oxide/carbon catalyst through carbonization. For details, 500 mg of Cu–TCPP was placed in a porcelain boat and heated to 450 °C at a heating rate of 2 °C min^{-1}, and then kept the heating process at 450 °C for 2 h. Subsequently, the product was naturally cooled to room temperature. Notably, the entire process was conducted under N_2 flow. The final black powder was referred to as $Cu_2O@NC$.

Experimental and analysis methods

Typically, 3 mg of the as-prepared catalyst was added to 100 mL of propofol solutions ($C_0 = 20$ mg L^{-1}) followed by stirring for 2 h to reach the adsorption equilibrium, then 30 mg of PMS was added. At the prescribed time intervals, a certain volume of the solution was taken out to measure the residue concentration of propofol in water using the high-performance liquid chromatography (HPLC) method.

HPLC. For propofol, the chromatographic separation was performed on a ZORBAX Eclipse C-18t analytical column (25 cm length; 4.6 mm internal diameter; 1.8 μm particle diameter) accompanied by a UV detector, and a wavelength set at 269 nm. The mobile phase consisted of A (0.1% of phosphoric acid in water) and B (acetonitrile) with a ratio of $V_A : V_B = 20 : 80$, and the flow rate was set to 1.0 mL min^{-1}. For NFX, the volume ratio of the mobile phase was changed to $V_A : V_B = 87 : 13$, and the wavelength was changed to 285 nm. For AMX, the volume ratio of the mobile phase was changed to $V_A : V_B = 25 : 75$, and the wavelength was changed to 230 nm. For CPX, the volume ratio of the mobile phase was set to $V_A : V_B = 25 : 75$, and the wavelength was changed to 262 nm.

LC-MS. The degradation products were analyzed using LC-MS (Agilent 1290 UPLC-QTOF 6550). The chromatographic separation was carried on a Waters Cortecs C-18t analytical column (2.1, 50 mm; 1.7 μm particle diameter). The mass spectra scanning range was set to 50–180 m/z. The drying gas flow was set to 15 L min^{-1}, and the sheath gas temperature was set to 350 °C with a flow of 12 L min^{-1}. The working voltage was set to 3500 V. The mobile phase consisted of A (0.1% formate in water) and B (acetonitrile), and the time-dependent ratios of A and B are displayed in Table 1:

GC-MS. GC-MS was used to analyze the degradation products of propofol as well, which was performed on a Shimadzu 2020 with an HP-5MS (30 m*0.25 mm*0.25 μm) instrument. The split injection separation ratio was set to 10, and the volume was 1 μL. The gas flow of the column was set to 1 mL min^{-1}. The

Table 1 The time-dependent composition of the mobile phase

Time/min	A (%)	B (%)
0	90	10
1	90	10
8	10	90
12	10	90
12.1	90	10
13	90	10

retention time was set to 1 min. The *m/z* scanning range was set as 25–200. The working temperature of the column was set to 280 °C.

Calculation method

The quantum chemistry calculation was performed on the software of Gauss 16 with a working method of b3lyp/6-311g. The correction factor was set as 0.9882. All the bond energies were calculated after optimizing the propofol molecule. All the energies of the molecule were studied at 298.15 K in a confined environment.

Results and discussion

Characterization

After incubation for 24 h, the resulting precipitates presented two-dimensional nanosheets. The SEM image (Fig. 1a) indicated that the Cu–TCPP nanosheet possesses a size of 500 nm, and the TEM image (Fig. 1c) revealed that the nanosheets possess pretty excellent light transmission properties, while the

HR-TEM image (Fig. 1e) showed fuzzy lattice stripes, which correspond with those previously reported for MOFs.[21,36] After pyrolysis, the morphology of the sample remains mostly unchanged, with slight aggregation (Fig. 1b), and the TEM image showed better light transmission (Fig. 1d). However, many particles were observed on the nanosheets, the HR-TEM image showed clear lattices with a spacing of 0.24 nm, which corresponds to the (1 1 1) plane of Cu_2O.[37–39] The elemental mapping graphs (Fig. $1g_{1–5}$) show that C, N, and O are highly overlapped, which demonstrates that 2D nanocomposites mainly consisted of three elements. The distribution of Cu mainly corresponded to the particle embedded in the nano-sheets. Given the lattice spacing, the doped particles were supposed to be Cu_2O.

XRD patterns were collected to investigate the crystal changes of Cu–TCPP before and after pyrolysis. It is observed that the dominant characteristic peaks were located at 7.8, 9.0 and 19.6° (Fig. 2a), which strongly corresponded to Cu–TCPP, thus demonstrating the successful assembly of 2D Cu–TCPP.[40–42] After pyrolysis, the characteristic peaks shifted to
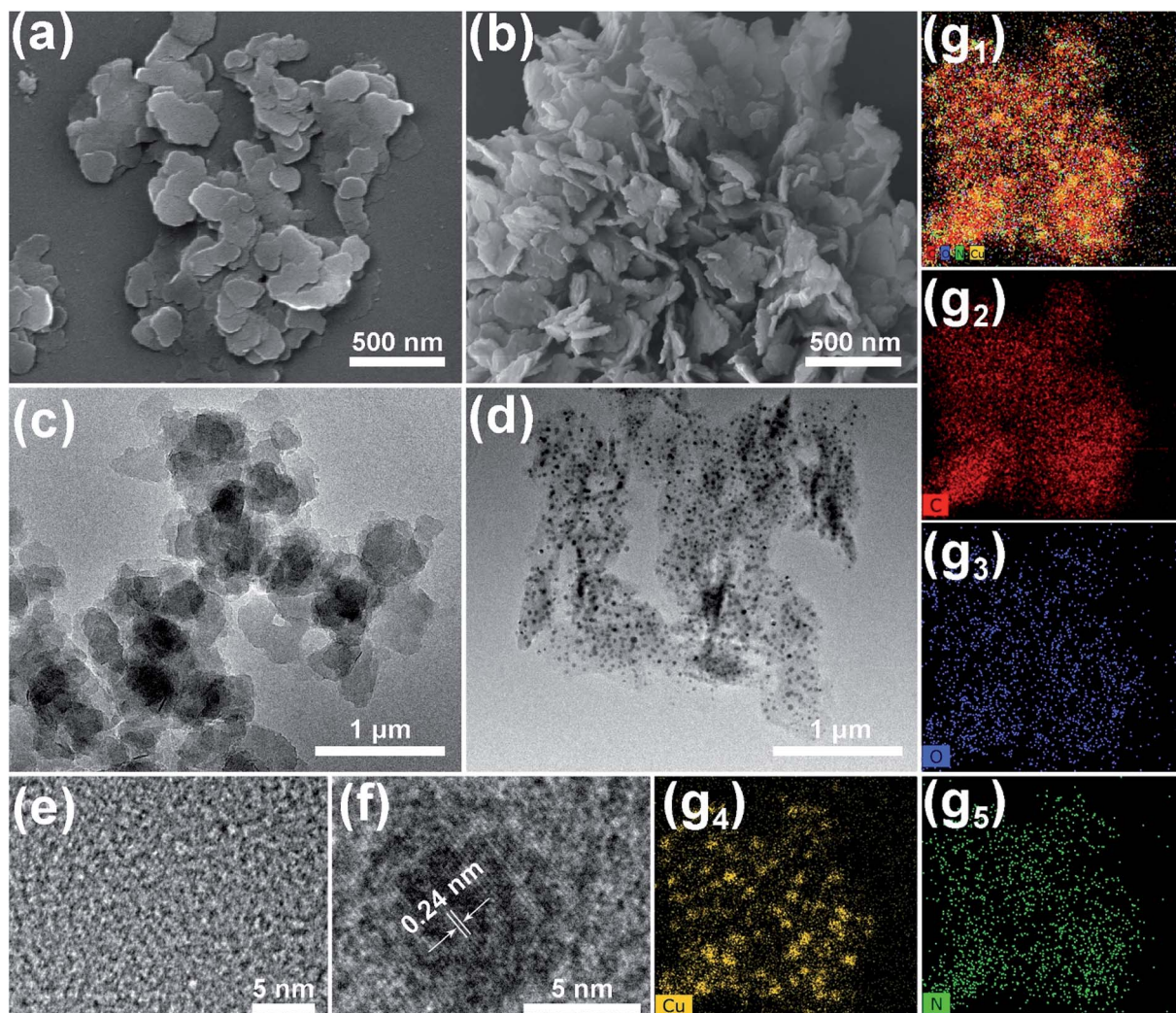

Fig. 1 The morphology of Cu−TCPP and Cu₂O@NC: SEM images of (a) Cu−TCPP and (b) Cu₂O@NC; TEM images of (c) Cu−TCPP and (d) Cu₂O@NC; HR-TEM images of (e) Cu−TCPP and (f) Cu₂O@NC; TEM-EDX results of Cu−TCPP, (g₁₋₅) general, C, O, Cu, N, respectively.
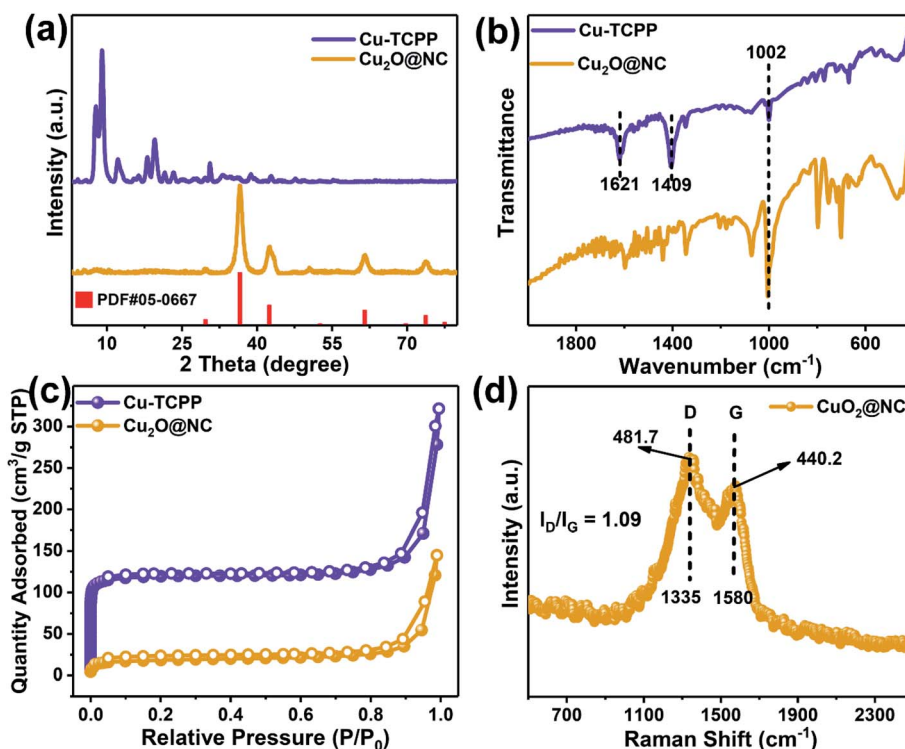
Fig. 2 (a) XRD patterns, (b) FTIR spectra, (c) the N$_2$ adsorption/desorption curves of Cu–TCPP and Cu$_2$O@NC, and (d) Raman spectra of Cu$_2$O@NC.

$36.5°$, $42.4°$, $61.6°$, $73.6°$, which completely corresponded to the standard pattern of Cu$_2$O.[37,43,44] The XRD pattern of the pyrolyzed products strongly corresponded to the HR-TEM image.

The FTIR spectra were employed to investigate the coordination mode between clusters and ligands. As shown in Fig. 2b, the two dominant peaks located at 1621 and 1409 cm^{-1} with $\Delta\nu$ > 200 cm^{-1} ($\nu_{asym} - \nu_{sym} = 212$ cm^{-1}), which was attributed to the carboxyl groups, indicating that the bridging bidentate was the main coordination mode between the metal clusters and the

ligands.[21,45] The spectra of the pyrolyzed product showed all chaotic peaks except for the sharp peak located at 1002 cm^{-1}, which corresponded to Cu–O, indicating that most Cu–TCPP was decomposed by the pyrolysis process.[46]

The surface area of the pristine MOF and derivative was analyzed by the Brunauer–Emmett–Teller (BET) method, the results showed that the Cu–TCPP had a larger surface area of 391.2 m^2 g^{-1}, while Cu$_2$O@NC had a smaller surface area of 189.3 m^2 g^{-1}. The porosities were analyzed by Barrett–Joyner–
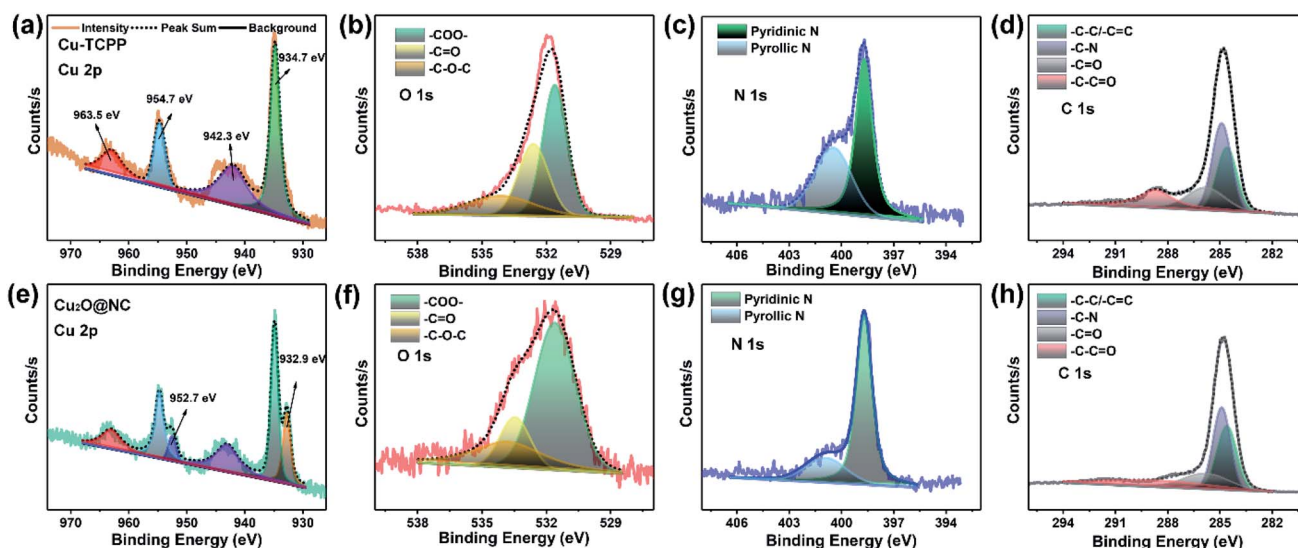

Fig. 3 The high-resolution spectra of (a) and (e) Cu 2p, (b) and (f) O 1s, (c) and (g) N 1s, (d) and (h) C 1s of Cu–TCPP and Cu$_2$O@NC.

Halenda (BJH) method, the results showed that the total pore volume was dramatically reduced by the pyrolysis process (Fig. S2†). As shown in Fig. 2c, the micropore was sharply reduced after pyrolysis. However, the average pore size was greatly expanded from 2.89 nm to 5.67 nm. These results demonstrated that the pyrolysis process could largely reduce the surface area, but also enlarge the pore size, which was beneficial to the mass transfer during the catalytical application.[47–49]

Raman shift was introduced to evaluate the defect and graphitic degree of the sample. The relative intensity ratio of the defect band (D, 1335 cm^{-1}) and graphitic band (G, 1580 cm^{-1}) was calculated as $I_D/I_G = 1.09$ (Fig. 2d), which indicated that the carbonized sample owned a large amount of the defect that may be beneficial to catalytic applications.[50,51]

The XPS spectra provided critical evidence for the investigation of the valence states of the elements. The survey spectra showed that all the elements were maintained after pyrolysis (Fig. S3†). For Cu 2p in the Cu–TCPP (Fig. 3a), the deconvoluted peaks located at 934.7 and 954.7 eV, are corresponding to Cu(I). The peaks centered at 942.3 and 963.5 eV are ascribed to Cu(II).[21,52] After pyrolysis (Fig. 3e), two new peaks centered at 932.9 and 952.7 eV were seen, which corresponded to Cu(I).[53,54] The spectrum of Cu 2p demonstrated that the co-existence of Cu(I) and Cu(II) both in Cu–TCPP and Cu₂O@NC, and Cu(II) gradually transferred to Cu(I) during the pyrolysis process. The spectrum of O 1s was largely weakened (Fig. 3b and f), which corresponded to the decomposition of carboxyl groups. The positive shift of O 1s was ascribed to an increase in the O vacancy. The spectrum of N 1s showed a decrease of pyrrolic N

after pyrolysis (Fig. 3c and g), which meant that N doping in carbon was mainly in the state of pyridinic N. The spectra of C 1s clearly showed a decrease in C in the carboxyl state.

Given all characterizations, a possible assembly-pyrolysis process could be established. Under hydrothermal ambient conditions, TCPP ligands were coordinated with Cu–O clusters to form Cu–TCPP nanosheets. When the as-prepared percussor was treated at high temperature in an N₂ flow, it gradually carbonized. The partial Cu(II) in the MOF was reduced to be Cu(I) in the state of Cu₂O. N was doped in carbon in the state of pyridinic N. Moreover, the morphology of the precursor was perfectly reserved. Although the pyrolysis process greatly reduced the surface area, it simultaneously enlarged the pore size of the carbonized product, which was much better for the mass transfer in the following catalysis process.

Removal performance

Removal efficiency. The as-prepared Cu₂O@NC nanosheets were introduced as catalysts to activate PMS during AOP leading propofol degradation. Initially, several control experiments were conducted to investigate the self-degradation ability of propofol. As shown in Fig. 4a, the concentration of propofol did not decrease under stirring, which demonstrated that propofol did not have the ability to self-degrade under this condition. When single Cu–TCPP or Cu₂O@NC was added, the concentration of propofol showed a slight decrease, which was attributed to the unsaturated adsorption capacity of the catalyst. It was difficult for PMS alone to remove propofol effectively, it could only remove about 25% of propofol within 60 min. The
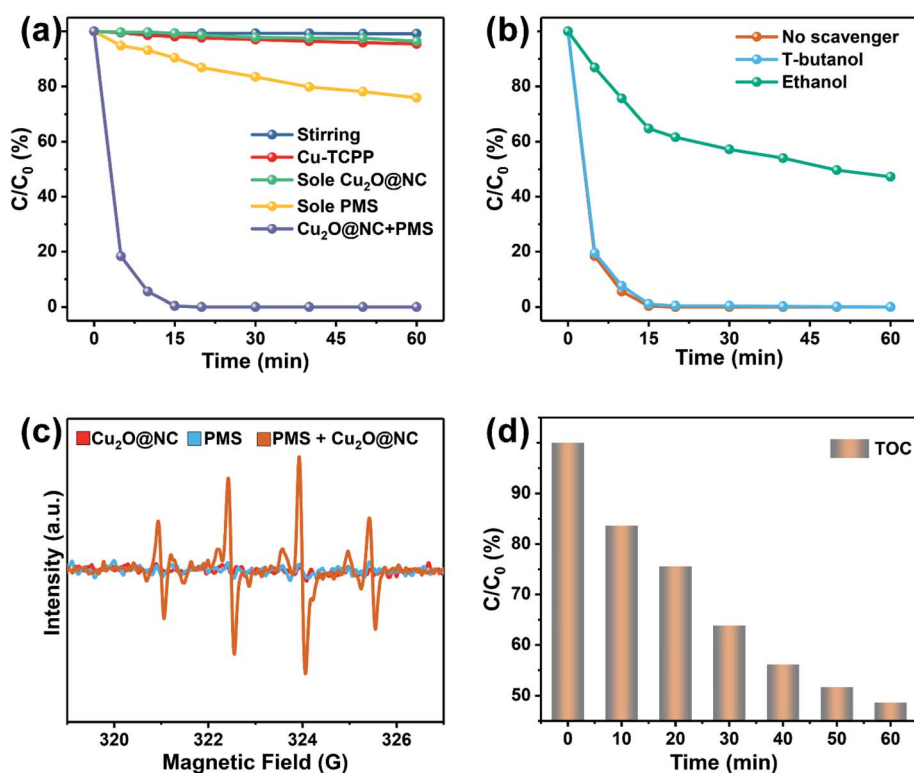

Fig. 4 The removal performance of PMS/Cu₂O@NC: (a) control experiments; (b) the trapping experiments; (c) ESR results; and (d) TOC results.
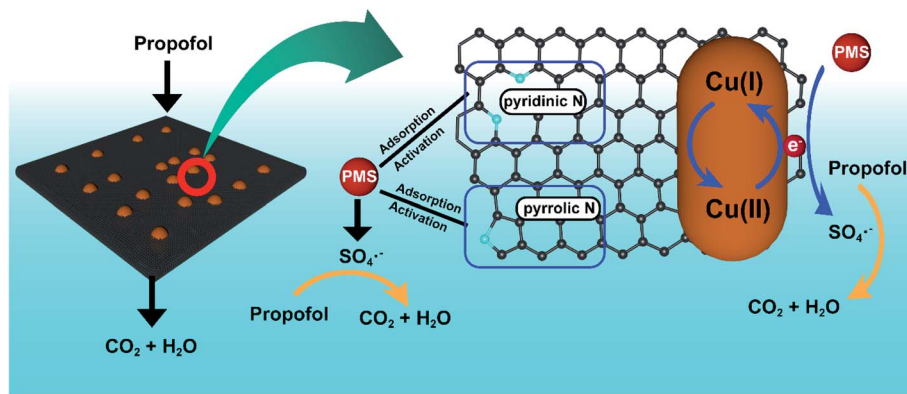
Fig. 5 The schematic illustration of the propofol degradation.

Table 2 The E, U_0, U, H and G at 298 K for the propofol (kJ mol^{-1}, H_2O)

	E	U_0	U	H	G
Value	−541.71	−541.44	−541.42	−541.42	−541.48

inferior removal ability was due to the oxidation ability of PMS. When PMS + Cu$_2$O@NC was added, the removal rate was dramatically high. Significantly, the system could remove propofol and bring it to the ultralow level within 15 min. In order to get an in-depth understanding of the catalytic performance of the PMS/Cu$_2$O@NC system, the initial reaction ($t \leq 20$ min) constant k was introduced (Fig. S4†). The fitting result showed that the value of k was in the order of k (PMS/Cu$_2$O@NC, 0.2759 min^{-1}) > k (PMS, 0.0044 min^{-1}) > k (Cu$_2$O/NC, 0.000276 min^{-1}) > k (stirring, 0.000318 min^{-1}). In addition, k (PMS/Cu$_2$O@NC) was much higher than the sum of k (PMS) and k (Cu$_2$O/NC), which demonstrated the synergistic catalytic effect of PMS and Cu$_2$O@NC. The results demonstrated that Cu$_2$O@NC has outstanding activation properties for PMS, thus accelerating the removal speed and rate of propofol to a great extent.

Mechanism. The main reactive oxidation species (ROS) that dominated the degradation process were investigated simultaneously. The hydroxyl radicals ($^{\bullet}$OH) and sulfate radicals (SO$_4^{\bullet-}$) were regarded as common radicals in PMS leading AOPs. Then, t-butanol and ethanol were introduced as the scavengers of $^{\bullet}$OH and SO$_4^{\bullet-}$, respectively. The scavengers could rapidly react with the radicals, so as to achieve the goal of quenching the radicals in the propofol removal process. As shown in Fig. 4b, t-butanol exhibited almost no quenching effect toward the process. The slight inhibitory effect was attributed to the t-butanol-induced change in the surface properties of the catalyst. Since ethanol could largely reduce the removal efficiency of the system, it indicated that SO$_4^{\bullet-}$ played a crucial role in the whole removal process.

To gain further understanding of ROS in the removal process, ESR measurements were introduced to analyze the generation of the radicals. As shown in Fig. 4c, there were almost no signals in the spectrum of a single Cu$_2$O@NC or PMS, while the signals of $^{\bullet}$OH and SO$_4^{\bullet-}$ in the spectrum of Cu$_2$O@NC + PMS were rather strong. These results indicated that Cu$_2$O@NC could promote PMS to produce $^{\bullet}$OH and SO$_4^{\bullet-}$ in an aqueous environment. To evaluate the thoroughness of the degradation of propofol, and TOC was introduced to test the degree of mineralization. As shown in Fig. 4d, the TOC was reduced to about 50%, indicating that the system could effectively degrade propofol to inorganic carbon (CO$_2$ and CO$_3^{2-}$).

A possible mechanism could be established based on the above results (Fig. 5). After pyrolysis, a large amount of N, including pyridinic N and pyrrolic N was doped on the carbon planes. N species showed excellent adsorption and activation capability toward PMS. Meanwhile, Cu$_2$O also presented certain defects on the surface of nanocomposites. Since PMS was added, a significant amount of SO$_4^{\bullet-}$ was produced, which then acted on propofol. Finally, propofol was degraded to CO$_2$ and H$_2$O.

Degradation pathway. In order to gain a further understanding of the degradation behavior of propofol, the quantum chemistry calculation was introduced in this work to evaluate the stability of the propofol molecule. As calculated, values of the electronic energy (E), zero-point (U_0), thermal energy (U), enthalpy (H) and Gibbs free energy (G) are displayed in Table 2:

Among all parameters, G was the most important parameter for predicting the stability of the target substance. The value of U was −541.48 kJ mol^{-1}, which meant the propofol molecule was rather stable and hardly oxidized under ambient conditions.[55–57]

At the same time, the bond energy was calculated under the same condition, which could be used to predict the degradation

Table 3 The theoretical bond energy in the propofol molecule

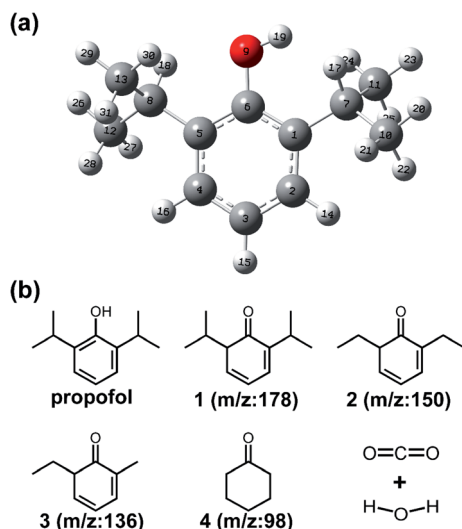| Site	Atom	BE (kJ mol^{-1})
1	C5–C8	455.8067
2	C8–C13	412.2012
3	C8–C12	439.3526
4	O9–H19	372.0118
5	C1–C7	448.6867
6	C7–C11	410.086
7	C7–C10	438.7031

Fig. 6 (a) The optimized chemical structure of propofol; (b) The deduced degradation pathway and possible degradation byproducts of propofol.

C8–C13 have comparable bond energies greater than those in O9–H19. It indicated that the two C–C bonds were subsequently destroyed by the radicals (Fig. S5a†). Given this, a substance with *m/z* of 150 appearing in the GC-MS and LC-MS (Fig. S5c†) should correspond to product **2** (2,6-diethylcyclohexa-2,4-dienone). Then, C7–C10 and C8–C12 showed greater bond energies, which meant they were more difficult to be destroyed, therefore correspond to the product of **3** (6-ethyl-2-methylcyclohexa-2,4-dienone). When the reactive substance continues to act on the organic pollutants, all C–C bonds were destroyed and all C=C bonds in the ring were reconstructed. The molar mass of 98 strongly corresponded to substance **4** (cyclohexanone, Fig. S5b†). The substance 4 was gradually oxidized to CO_2 and H_2O (Fig. 6b).

From TOC results, we knew that organic substances could not be clearly removed, and results of GC-MS and LC-MS demonstrated that the main byproduct was cyclohexanone. According to reports, cyclohexanone is a low-toxicity chemical with a pungent odor, which makes it easier to be noticed and stay away.[58–60]

Recyclability. The stability of the catalyst is essential for practical applications. Herein, cycle experiments were conducted to test the recyclability of the as-prepared Cu₂O@NC. The reduction of catalytic performance was tested with 5 cycles of the degradation process. The results showed that (Fig. 7a) although there was a certain degree of attenuation, the PMS/Cu₂O@NC still exhibited excellent catalytic performance even after 5 cycles of usage and could remove more than 95% of propofol in the same period. The SEM image (Fig. 7b) showed
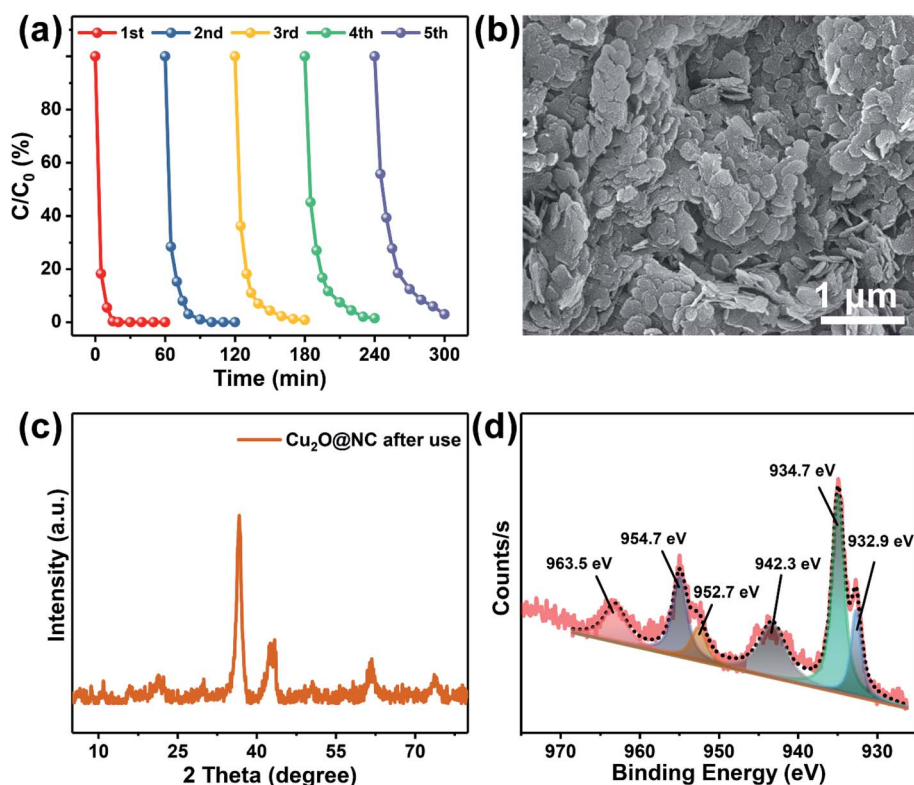
pathway and the byproducts. As shown in Table 3 and Fig. 6a, the bond of O9–H19 had the smallest bond energy (372.01 kJ mol⁻¹) compared with other bonds, which meant that the phenolic hydroxyl group was most easily oxidized to a quinone. According to reported works, the molar mass of the byproduct is 178, which corresponds to chemical **1** (2,6-diisopropylcyclohexa-2,4-dienone). The bonds in C7–C11 and

Fig. 7 (a) The cycle experiments, (b) SEM image, (c) XRD pattern and (d) Cu 2p spectra of the Cu₂O@NC after use.
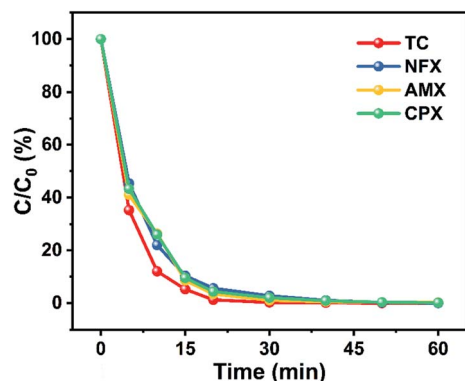
Fig. 8 The removal performance of the PMS/Cu$_2$O@NC toward TC, NFX, AMX, and CPX.

that the surface of Cu$_2$O@NC became rougher after use. The XRD pattern showed the same characteristic peaks as the green catalyst (Fig. 7c), which indicated that the catalyst had excellent stability. XPS spectra showed that the area ratio of Cu(II)/Cu(I) was slightly higher than that of the unused catalyst, which demonstrated that Cu(I) played a dominant role in activating PMS (Fig. 7d). All the results indicated that the as-prepared Cu$_2$O@NC exhibited outstanding stability during the catalytic process, which could support its further application in practical wastewater treatment.

Universality. The PMS/Cu$_2$O system was also used to study its effect on other commonly abused pharmaceuticals in the operating room wastewater. TC, NFX, AMX, and CPX are the most commonly used antibiotics that are frequently detected in the operating room wastewater. After long-term exposure to these pharmaceuticals, organisms are prone to a high risk of mutation.[61–63] As shown in Fig. 8, PMS/Cu$_2$O@NC could also remove >99% of TC, NFX, AMX and CPX within about 30 min, thus proving that the system had excellent universality for most commonly discharged antibiotics.

Conclusion

In this work, we demonstrated a novel strategy to remove propofol from operating room wastewater. In conclusion, the 2D Cu–TCPP nanosheets were assembled and employed as a pristine material to produce a 2D heterogeneous catalyst. The as-prepared catalyst exhibited excellent PMS activation performance, which could rapidly and effectively remove propofol and other abused antibiotics such as TC, NFX, AMX, and CPX. This work provides a potential method for treating operating room wastewater by the PMS leading AOP method.

Author contributions

Conceptualization, Y. T.; methodology, Y. T. and S. Z.; software, Y. T.; investigation, Y. T. and Z. P.; data curation, Z. L.; writing – original draft preparation, Y. T.; writing – review and editing, Y. T. and P. G.; supervision, P. G. and L. C.; project administration, Y. T., L. C. and P. G.

Conflicts of interest

There are no conflicts to declare.

Acknowledgements

References

1 S. Kaniyil, A. Krishnadas, A. K. Parathody and K. T. J. A. E. Ramadas, *Anesth. Essays Res.*, 2017, **11**, 304–308.

2 H. Beloeil and P. Albaladejo, *Best Pract. Res., Clin. Anaesthesiol.*, 2021, **35**, 83–91.

3 A. G. Parvatker, H. Tunceroglu, J. D. Sherman, P. Coish, P. Anastas, J. B. Zimmerman and M. J. Eckelman, *ACS Sustainable Chem. Eng.*, 2019, **7**, 6580–6591.

4 K. Chaudhary, R. Garg, A. R. Bhalotra, R. Anand and K. Girdhar, *J. Anaesthesiol., Clin. Pharmacol.*, 2012, **28**, 56–61.

5 K. Y. Nandiwale and V. V. Bokade, *RSC Adv.*, 2014, **4**, 32467–32474.

6 G. M. Yip, Z. W. Chen, C. J. Edge, E. H. Smith, R. Dickinson, E. Hohenester, R. R. Townsend, K. Fuchs, W. Sieghart, A. S. Evers and N. P. Franks, *Nat. Chem. Biol.*, 2013, **9**, 715–720.

7 P. Falas, H. R. Andersen, A. Ledin and J. la Cour Jansen, *Water Sci. Technol.*, 2012, **66**, 783–791.

8 R. F. Mankes, *Anesth. Analg.*, 2012, **114**, 1091–1092.

9 X. Li, P. Martinez-Lozano Sinues, R. Dallmann, L. Bregy, M. Hollmen, S. Proulx, S. A. Brown, M. Detmar, M. Kohler and R. Zenobi, *Angew. Chem., Int. Ed.*, 2015, **54**, 7815–7818.

10 S. F. Lane, *Br. J. Anaesth.*, 2020, **124**, e221–e222.

11 S. Klatte, H.-C. Schaefer and M. Hempel, *Sustainable Chem. Pharm.*, 2017, **5**, 61–66.

12 H. T. Nguyen, P. K. Thai, S. L. Kaserzon, J. W. O'Brien, G. Eaglesham and J. F. Mueller, *Sci. Total Environ.*, 2018, **631–632**, 469–475.

13 K. M. Blum, P. L. Andersson, L. Ahrens, K. Wiberg and P. Haglund, *Sci. Total Environ.*, 2018, **612**, 1532–1542.

14 M. Kostrubiak, C. M. Vatovec, L. A. Dupigny-Giroux, D. M. Rizzo, W. C. Paganelli and M. H. Tsai, *J. Med. Syst.*, 2020, **44**, 169.

15 Q. Du, X. Zhang, X. Zhang, M. Wei, H. Xu and S. Wang, *Artif. Cells, Nanomed., Biotechnol.*, 2019, **47**, 1265–1271.

16 X. Hu, J. M. T. Pierce, T. Taylor and K. Morrissey, *Resour., Conserv. Recycl.*, 2021, **167**, 105411.

17 S. O. Ganiyu, E. D. van Hullebusch, M. Cretin, G. Esposito and M. A. Oturan, *Sep. Purif. Technol.*, 2015, **156**, 891–914.

18 F. Martinez, M. J. Lopez-Munoz, J. Aguado, J. A. Melero, J. Arsuaga, A. Sotto, R. Molina, Y. Segura, M. I. Pariente, A. Revilla, L. Cerro and G. Carenas, *Water Res.*, 2013, **47**, 5647–5658.

19 F. J. Benitez, J. L. Acero, F. J. Real, G. Roldan and F. Casas, *Chem. Eng. J.*, 2011, **168**, 1149–1156.

20 S. Farhadi, B. Aminzadeh, A. Torabian, V. Khatibikamal and M. Alizadeh Fard, *J. Hazard. Mater.*, 2012, **219–220**, 35–42.

21 S. Zhao, S. Li, Z. Zhao, Y. Su, Y. Long, Z. Zheng, D. Cui, Y. Liu, C. Wang, X. Zhang and Z. Zhang, *Environ. Sci. Pollut. Res.*, 2020, **27**, 39186–39197.

22 H. N. Tran, F. Tomul, N. Thi Hoang Ha, D. T. Nguyen, E. C. Lima, G. T. Le, C. T. Chang, V. Masindi and S. H. Woo, *J. Hazard. Mater.*, 2020, **394**, 122255.

23 A. Majumdar and A. Pal, *Clean Technol. Environ. Policy*, 2019, **22**, 11–42.

24 M. J. Benotti, B. D. Stanford, E. C. Wert and S. A. Snyder, *Water Res.*, 2009, **43**, 1513–1522.

25 J. A. Garrido-Cardenas, B. Esteban-Garcia, A. Aguera, J. A. Sanchez-Perez and F. Manzano-Agugliaro, *Int. J. Environ. Res. Public Health*, 2019, **17**, 170.

26 A. H. Khan, N. A. Khan, S. Ahmed, A. Dhingra, C. P. Singh, S. U. Khan, A. A. Mohammadi, F. Changani, M. Yousefi, S. Alam, S. Vambol, V. Vambol, A. Khursheed and I. Ali, *J. Cleaner Prod.*, 2020, **269**, 122411.

27 V. Homem and L. Santos, *J. Environ. Manage.*, 2011, **92**, 2304–2347.

28 H. Gao, H. Yang, J. Xu, S. Zhang and J. Li, *Small*, 2018, **14**, 1801353.

29 C. V. Nguyen, Y.-T. Liao, T.-C. Kang, J. E. Chen, T. Yoshikawa, Y. Nakasaka, T. Masuda and K. C. W. Wu, *Green Chem.*, 2016, **18**, 5957–5961.

30 F. K. Shieh, S. C. Wang, C. I. Yen, C. C. Wu, S. Dutta, L. Y. Chou, J. V. Morabito, P. Hu, M. H. Hsu, K. C. Wu and C. K. Tsung, *J. Am. Chem. Soc.*, 2015, **137**, 4276–4279.

31 S. Akbari, J. Mokhtari and Z. Mirjafari, *RSC Adv.*, 2017, **7**, 40881–40886.

32 S. Zhao, S. Li, Y. Long, X. Shen, Z. Zhao, Q. Wei, S. Wang, Z. Zhang, X. Zhang and Z. Zhang, *Chemosphere*, 2021, **280**, 130637.

33 S. Jamalifard, J. Mokhtari and Z. Mirjafary, *RSC Adv.*, 2019, **9**, 22749–22754.

34 J. Mokhtari and A. Hasani Bozcheloei, *Inorg. Chim. Acta*, 2018, **482**, 726–731.

35 H. Zhang, X. Zheng, L. M. Yang and E. Ganz, *Inorg. Chem.*, 2021, **60**, 2656–2662.

36 S. Zhao, Z. Ding, C. Wang, S. Wang, S. Li, Z. Zhang and X. Zhang, *ACS Omega*, 2019, **4**, 14294–14300.

37 D. Jiang, J. Xue, L. Wu, W. Zhou, Y. Zhang and X. Li, *Appl. Catal., B*, 2017, **211**, 199–204.

38 S. Zhang, S. Zhang, F. Peng, H. Zhang, H. Liu and H. Zhao, *Electrochem. Commun.*, 2011, **13**, 861–864.

39 J. Liu, Z. Gao, H. Han, D. Wu, F. Xu, H. Wang and K. Jiang, *Chem. Eng. J.*, 2012, **185–186**, 151–159.

40 Y. Li, Z. Gao, F. Chen, C. You, H. Wu, K. Sun, P. An, K. Cheng, C. Sun, X. Zhu and B. Sun, *ACS Appl. Mater. Interfaces*, 2018, **10**, 30930–30935.

41 M. Zhao, Y. Wang, Q. Ma, Y. Huang, X. Zhang, J. Ping, Z. Zhang, Q. Lu, Y. Yu, H. Xu, Y. Zhao and H. Zhang, *Adv. Mater.*, 2015, **27**, 7372–7378.

42 D. T. Lee, J. D. Jamir, G. W. Peterson and G. N. Parsons, *Small*, 2019, **15**, e1805133.

43 A. Kerour, S. Boudjadar, R. Bourzami and B. Allouche, *J. Solid State Chem.*, 2018, **263**, 79–83.

44 H. Lahmar, F. Setifi, A. Azizi, G. Schmerber and A. Dinia, *J. Alloys Compd.*, 2017, **718**, 36–45.

45 G. B. Deacon and R. J. Phillips, *Coord. Chem. Rev.*, 1980, **33**, 227–250.

46 A. H. B. Dourado, A. G. M. da Silva, F. A. C. Pastrián, R. L. Munhos, A. P. de Lima Batista, A. G. S. de Oliveira-Filho, J. Quiroz, D. C. de Oliveira, P. H. C. Camargo and S. I. Córdoba de Torresi, *J. Catal.*, 2019, **375**, 95–103.

47 K. Wan, A.-d. Tan, Z.-p. Yu, Z.-x. Liang, J.-h. Piao and P. Tsiakaras, *Appl. Catal., B*, 2017, **209**, 447–454.

48 S. Tsujimura, M. Oyama, H. Funabashi and S. Ishii, *Electrochim. Acta*, 2019, **322**, 134744.

49 Q. Wu, X. Zhang, Y. Lv, L. Lin, Y. Liu and X. Zhou, *J. Mater. Chem. A*, 2018, **6**, 20347–20355.

50 J. C. Yoon, J. Hwang, P. Thiyagarajan, R. S. Ruoff and J. H. Jang, *ACS Appl. Mater. Interfaces*, 2017, **9**, 21457–21463.

51 P. Song, X. He, J. Tao, X. Shen, Z. Yan, Z. Ji, A. Yuan, G. Zhu and L. Kong, *Appl. Surf. Sci.*, 2021, **535**, 147755.

52 B. Li, X. Wang, L. Chen, Y. Zhou, W. Dang, J. Chang and C. Wu, *Theranostics*, 2018, **8**, 4086–4096.

53 X. Zhang, X. Cui, Y. Sun, K. Qi, Z. Jin, S. Wei, W. Li, L. Zhang and W. Zheng, *ACS Appl. Mater. Interfaces*, 2018, **10**, 745–752.

54 S.-Y. Yu, Y. Gao, F.-Z. Chen, G.-C. Fan, D.-M. Han, C. Wang and W.-W. Zhao, *Sens. Actuators, B*, 2019, **290**, 312–317.

55 T. Steinbrecher, C. Zhu, L. Wang, R. Abel, C. Negron, D. Pearlman, E. Feyfant, J. Duan and W. Sherman, *J. Mol. Biol.*, 2017, **429**, 948–963.

56 T. Hiemstra, *Geochim. Cosmochim. Acta*, 2015, **158**, 179–198.

57 A. Lenz and L. Ojamäe, *Chem. Phys. Lett.*, 2006, **418**, 361–367.

58 C. H. Lim, Y. H. Lee, Y. S. Kim, H. S. Choi and D. S. Seo, *Inhalation Toxicol.*, 2018, **30**, 247–254.

59 A. M. Api, D. Belsito, D. Botelho, M. Bruze, G. A. Burton Jr, J. Buschmann, M. L. Dagli, M. Date, W. Dekant, C. Deodhar, M. Francis, A. D. Fryer, L. Jones, K. Joshi, S. La Cava, A. Lapczynski, D. C. Liebler, D. O'Brien, A. Patel, T. M. Penning, G. Ritacco, J. Romine, N. Sadekar, D. Salvito, T. W. Schultz, I. G. Sipes, G. Sullivan, Y. Thakkar, Y. Tokura and S. Tsang, *Food Chem. Toxicol.*, 2019, **134**, 110604.

60 C. Liu, X. Li, Y. Li and X. Wen, *Water, Air, Soil Pollut.*, 2020, **231**, 331.

61 G. K. Paulus, L. M. Hornstra, N. Alygizakis, J. Slobodnik, N. Thomaidis and G. Medema, *Int. J. Hyg. Environ. Health*, 2019, **222**, 635–644.

62 Q. Wang, P. Wang and Q. Yang, *Sci. Total Environ.*, 2018, **621**, 990–999.

63 E. Szekeres, A. Baricz, C. M. Chiriac, A. Farkas, O. Opris, M. L. Soran, A. S. Andrei, K. Rudi, J. L. Balcazar, N. Dragos and C. Coman, *Environ. Pollut.*, 2017, **225**, 304–315.